Observations of Vertical Wind Shear Heterogeneity in Convective Boundary Layers

PAUL MARKOWSKI AND YVETTE RICHARDSON

Department of Meteorology, The Pennsylvania State University, University Park, Pennsylvania

(Manuscript received 7 November 2005, in final form 11 July 2006)

ABSTRACT

Dual-Doppler wind syntheses from mobile radar observations obtained during the International H_2O Project document some of the spatial variability of vertical wind profiles in convective boundary layers. Much of the variability of popular forecasting parameters such as vertical wind shear magnitude and storm-relative helicity is thought to result from pressure and temperature gradients associated with mesoscale boundaries (e.g., drylines, outflow boundaries, fronts). These analyses also reveal substantial heterogeneity even in the absence of obvious mesoscale wind shifts—in regions many might have classified as "horizontally homogeneous" with respect to these parameters in the past. This heterogeneity is closely linked to kinematic perturbations associated with boundary layer convection. When a mean wind is present, the large spatial variability implies significant temporal variability in the vertical wind profiles observed at fixed locations, with the temporal variability increasing with mean wind speed. Significant differences also can arise between true hodographs and "pseudohodographs" obtained from rawinsondes that are advected horizontally as they ascend. Some possible implications of the observed heterogeneity with respect to forecasting and simulating convective storms also are discussed.

1. Introduction

The heterogeneity of the thermodynamic and kinematic state of the atmosphere has received increased appreciation in the last decade within the severe storms community, likely due in part to dense observations obtained from some recent field experiments as well as recent simulation studies demonstrating the sensitivity of convective storms to small thermodynamic and wind shear perturbations (e.g., Richardson 1999; McCaul and Weisman 2001; McCaul and Cohen 2002; James et al. 2006; Richardson et al. 2007). Weckwerth et al. (1996) have shown that the thermodynamic variability observed among soundings within the boundary layer strongly depends on whether the sounding is launched through the updraft or downdraft of circulations induced by boundary layer convective overturning. Soundings launched through a boundary layer updraft depicted deeper, richer moist layers, implying less convective inhibition (CIN) and larger convective available potential energy (CAPE) than nearby soundings launched through a boundary layer downdraft, where lesser moisture concentrations and relatively shallow moist layers were indicated. Brooks et al. (1996) have documented substantial thermodynamic heterogeneity revealed by soundings launched during the Verification of the Origins of Rotation in Tornadoes Experiment (VORTEX; Rasmussen et al. 1994). Markowski et al. (1998) also have documented heterogeneity revealed by VORTEX soundings, but in the storm-relative helicity (SRH) values derived from the sounding wind profiles. It is difficult to determine to what degree the variability documented by Brooks et al. and Markowski et al. was due to meso-β-scale processes (e.g., baroclinic vorticity generation along an outflow boundary) versus meso-γ-scale processes (e.g., boundary layer convection).

The purpose of this article is to present a better characterization of the heterogeneity present in environments favorable for convective storms than can be gleaned from soundings alone.[1] Our goal is to document the spatial and temporal variability of vertical wind profiles in convective boundary layers and to relate this variability to the organization of boundary

Corresponding author address: Dr. Paul Markowski, Department of Meteorology, The Pennsylvania State University, 503 Walker Building, University Park, PA 16802.
E-mail: pmarkowski@psu.edu

[1] An earlier version of this work was presented at the American Meteorological Society's 22d Conference on Severe Local Storms (Markowski and Richardson 2004).

DOI: 10.1175/MWR3334.1

layer convection. What follows below are analyses derived from four ground-based mobile radar datasets obtained during the International H_2O Project (IHOP; Weckwerth et al. 2004). An overview of these data and the wind synthesis methods is provided in the next section. Sections 3–5 contain examples of the time and space variability of hodographs and the vertical wind shear parameters derived from them. Some closing remarks pertaining to future research are provided in section 6.

2. Data and analysis techniques

a. Case descriptions

This paper presents examples of vertical wind profile heterogeneity from four IHOP cases in 2002: 10, 12, 14, and 19 June. Three of the datasets (10, 12, and 19 June) were obtained during missions targeting convection initiation; thus, the environments tended to have appreciable CAPE (>1000 J kg^{-1}) and relatively small CIN (<50 J kg^{-1}). Mesoscale boundaries (e.g., fronts, drylines, outflow boundaries) also were present in these three cases. The fourth case (14 June) did not have a significant potential for convection initiation and was characterized by weak synoptic and mesoscale pressure and temperature gradients. In all four cases, partly to mostly sunny conditions prevailed, with deep, well-mixed, convective boundary layers as indicated by mobile soundings and the dual-Doppler vertical velocity retrievals. Peak boundary layer updrafts, often organized into cells or rolls as is commonly the case in a convective boundary layer, ranged from 3 to 6 m s^{-1} at 1 km above ground level (AGL). Additional details are summarized below.

1) 10 JUNE 2002

The 10 June case featured a weak cold front in central Kansas (Fig. 1a). The boundary layer ahead of the front was characterized by open cellular convection at the 2036 UTC analysis time (Fig. 1b). Behind the front, boundary layer drafts were arranged in quasi-linear bands. It was not clear whether these structures were due to horizontal convective rolls (HCRs) or waves along the frontal surface. Shallow cumulus clouds were observed on both sides of the front. Scattered cumulonimbus clouds developed along the front near the analysis domain within 30 min of the analyses presented herein (~2100 UTC). A more complete summary of this case is presented by Arnott et al. (2006).

2) 12 JUNE 2002

The analysis domain at 1945 UTC 12 June 2002 was approximately bisected in the west–east direction by an outflow boundary that was produced by thunderstorms occurring during the overnight hours (Fig. 2a). A dryline was present in the warm sector south of the outflow boundary near the center of the domain. Westward-propagating gravity waves were observed in the outflow air mass. There is some weak suggestion of organization into rolls and cells at some analysis times, especially on the warm side of the outflow boundary, although Weckwerth et al. (1997) would probably classify the convection as being disorganized on average (Fig. 2b). Shallow cumulus clouds were observed within the data analysis region at the times analyzed herein, although some towering cumulus clouds developed along the outflow boundary at later times (2100–2130 UTC). Cumulonimbus clouds were initiated east of the analysis region along the dryline during the same time period. A more complete summary of this case is presented by Markowski et al. (2006).

3) 14 JUNE 2002

The 14 June case nicely illustrates the heterogeneity present in the absence of significant large-scale pressure and temperature gradients (Fig. 3a). Weak vertical wind shear ($<2.5 \times 10^{-3}$ s^{-1}), weak mean wind speeds (1–2 m s^{-1}), and cloud-free skies were present at the 1755 UTC analysis time. Small cumulus clouds developed within the analysis domain later in the day. HCRs developed several hours after sunrise. The HCRs became ill defined and were replaced by cellular structures by approximately midday (1700 UTC). The cellular structures persisted well past the time of the analysis presented herein (1755 UTC). The cellular nature of the boundary layer convection is more apparent in the raw radar reflectivity data (not shown) than in the vertical velocity field retrieved by the dual-Doppler wind synthesis (Fig. 3b), likely because of the smoothing inherent in the objective analysis and wind synthesis and the fact that the correlation between radar reflectivity and vertical velocity tends to be significantly less than unity [correlations of 0.4–0.6 have been documented by B. Geerts (2004, personal communication), Markowski et al. (2006), and Stonitsch and Markowski (2007)].

4) 19 JUNE 2002

A dryline was the focus of data collection efforts on 19 June. Analyses are presented at 2030 UTC, near the time that convection was initiated along the dryline (Fig. 4a; Richardson et al. 2004; Murphey et al. 2006). Relatively large mean wind speeds (>12 m s^{-1}) were present east of the dryline within the boundary layer. The boundary layer convection east of the dryline tended to be disorganized (i.e., not organized into

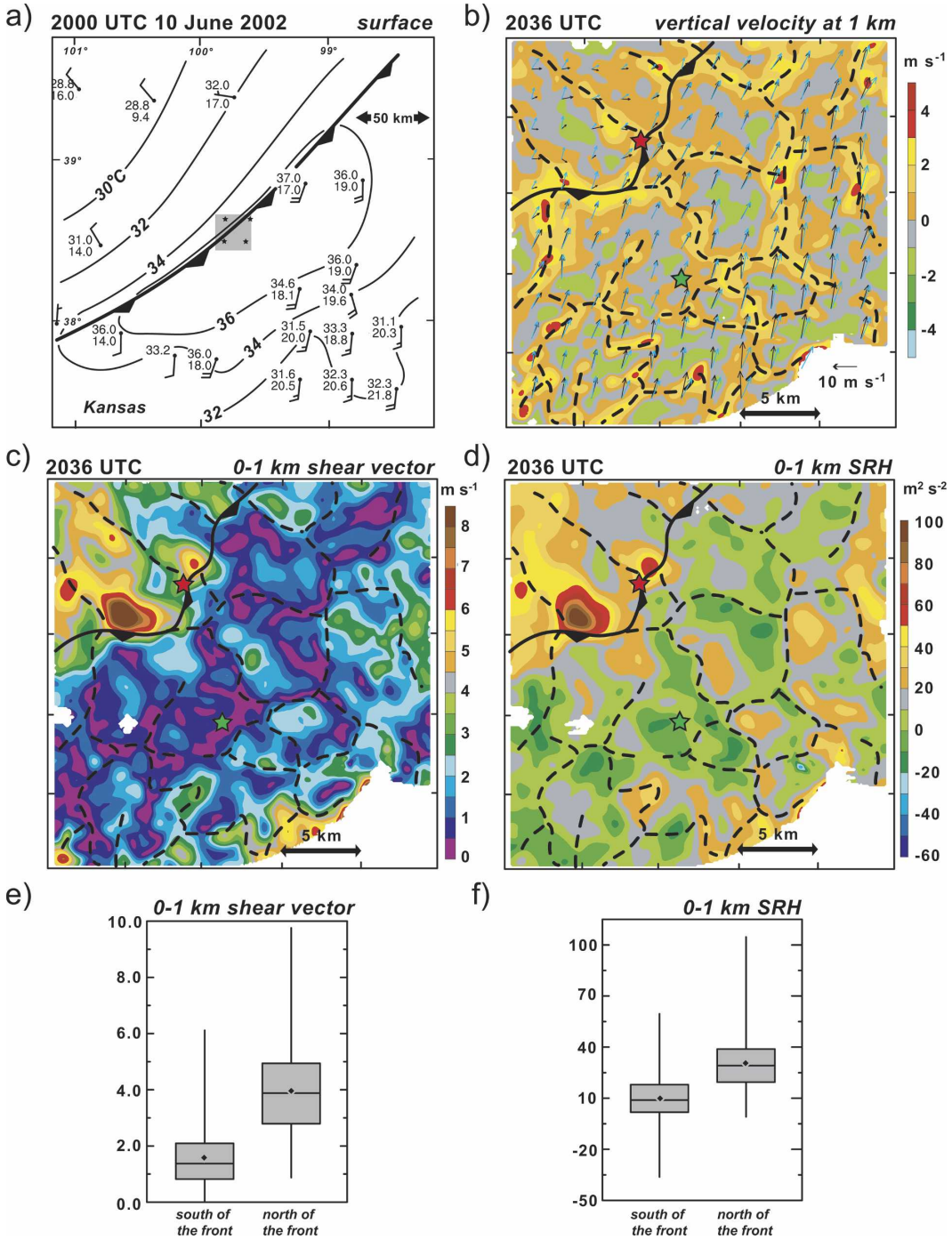

FIG. 1. (a) Surface analysis at 2000 UTC 10 Jun 2002. Isotherms (°C) are drawn at 2°C intervals, station models indicate temperature and dewpoint (°C), and wind barbs indicate wind velocity (half barb—2.5 m s^{-1}, full barb—5 m s^{-1}). The cold front is indicated using conventional symbols. The gray box indicates the location of the multiple-Doppler wind synthesis domain, and the stars indicate the locations of the mobile radars used in the wind synthesis. (b) Horizontal cross section of vertical velocity at 1 km AGL at 2036 UTC 10 Jun 2002. Horizontal wind vectors at the lowest grid level (black) and at 1.0 km (light blue) also are overlaid (the tail of each vector is located at every 18th grid point). Dashed lines highlight regions of contiguous boundary layer updraft. The green and red stars indicate the locations of the hodographs displayed in Figs. 12a,b, respectively. (c) Horizontal cross section of the magnitude of the 0–1-km wind shear vector S at 2036 UTC 10 Jun 2002. As in (b), the green and red stars indicate the locations of the hodographs displayed in Figs. 12a,b, respectively. (d) Horizontal cross section of the SRH in the 0–1 km AGL layer at 2036 UTC 10 Jun 2002. Storm motion was estimated using the Bunkers et al. (2000) method, based on mobile soundings launched within the analysis domain. As in (b) and (c), the green and red stars indicate the locations of the hodographs displayed in Figs. 12a,b, respectively. (e) Box-and-whisker plot for the magnitudes of the 0–1-km wind shear vector, partitioned by air mass. The small diamonds indicate the sample means. (f) Same as in (e), but for the 0–1-km SRH.

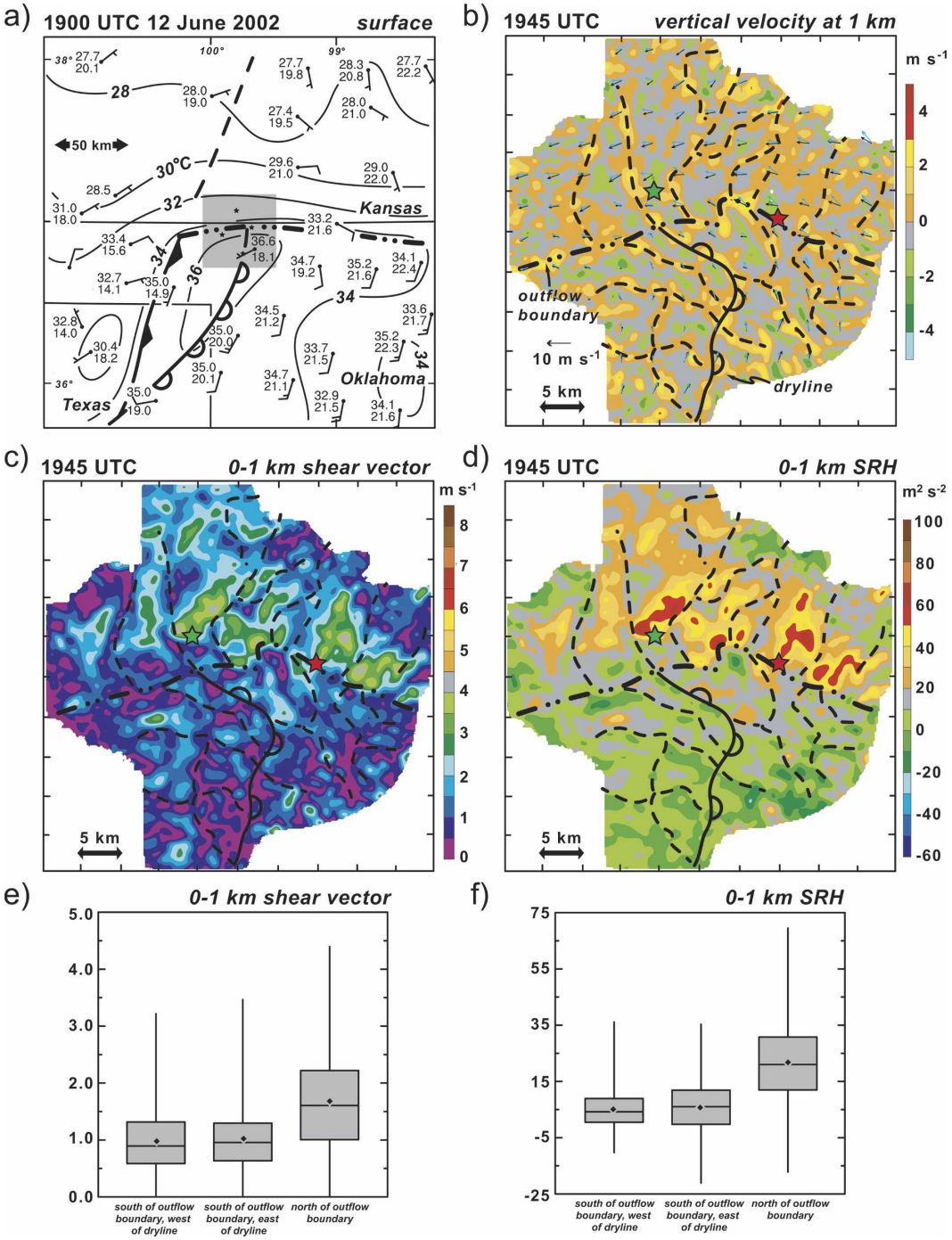

FIG. 2. Same as in Fig. 1, but for 12 Jun 2002. The surface analysis is from 1900 UTC, and the vertical velocity, 0–1-km shear vector magnitude *S*, and SRH analyses are from 1945 UTC. The dash–dot line indicates an outflow boundary and the line with unfilled scallops indicates a dryline. (a) The dashed line indicates the position of a trough of low pressure. (b)–(d) The green and red stars indicate the locations of the hodographs displayed in Figs. 12c,d, respectively.

clearly identifiable cells or rolls; Fig. 4b). West of the dryline, HCRs were visible in both the dual-Doppler vertical velocity retrievals and in the radar reflectivity fields (not shown). Updrafts along the dryline occasionally were quite strong, with peak values exceeding 5 m s^{-1}. Numerous misocyclones also were observed along the dryline. A more detailed study of their role in modulating the vertical velocity field (and the associ-

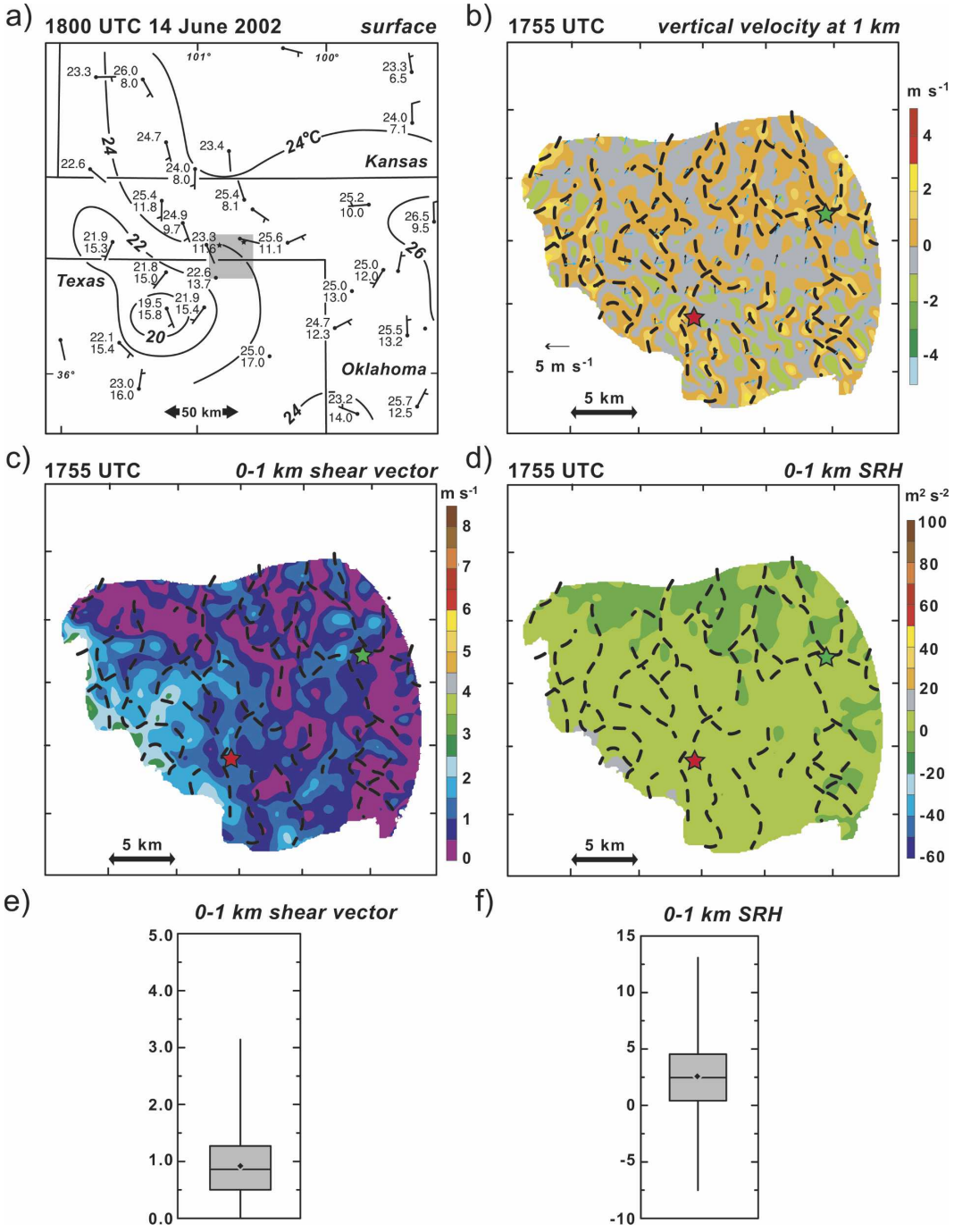

FIG. 3. Same as in Fig. 1, but for 14 Jun 2002. The surface analysis is from 1800 UTC, and the vertical velocity, 0–1-km shear vector magnitude *S*, and SRH analyses are from 1755 UTC. (b)–(d) The green and red stars indicate the locations of the hodographs displayed in Figs. 12e,f, respectively.

ated implications for convection initiation) is presented in a separate paper by Murphey et al. (2006) and also will be the subject of a future article by one of the authors herein (Marquis et al. 2007).

b. Multi-Doppler wind syntheses

A mobile radar network consisting of two Doppler on Wheels (DOW) radars (Wurman et al. 1997), the

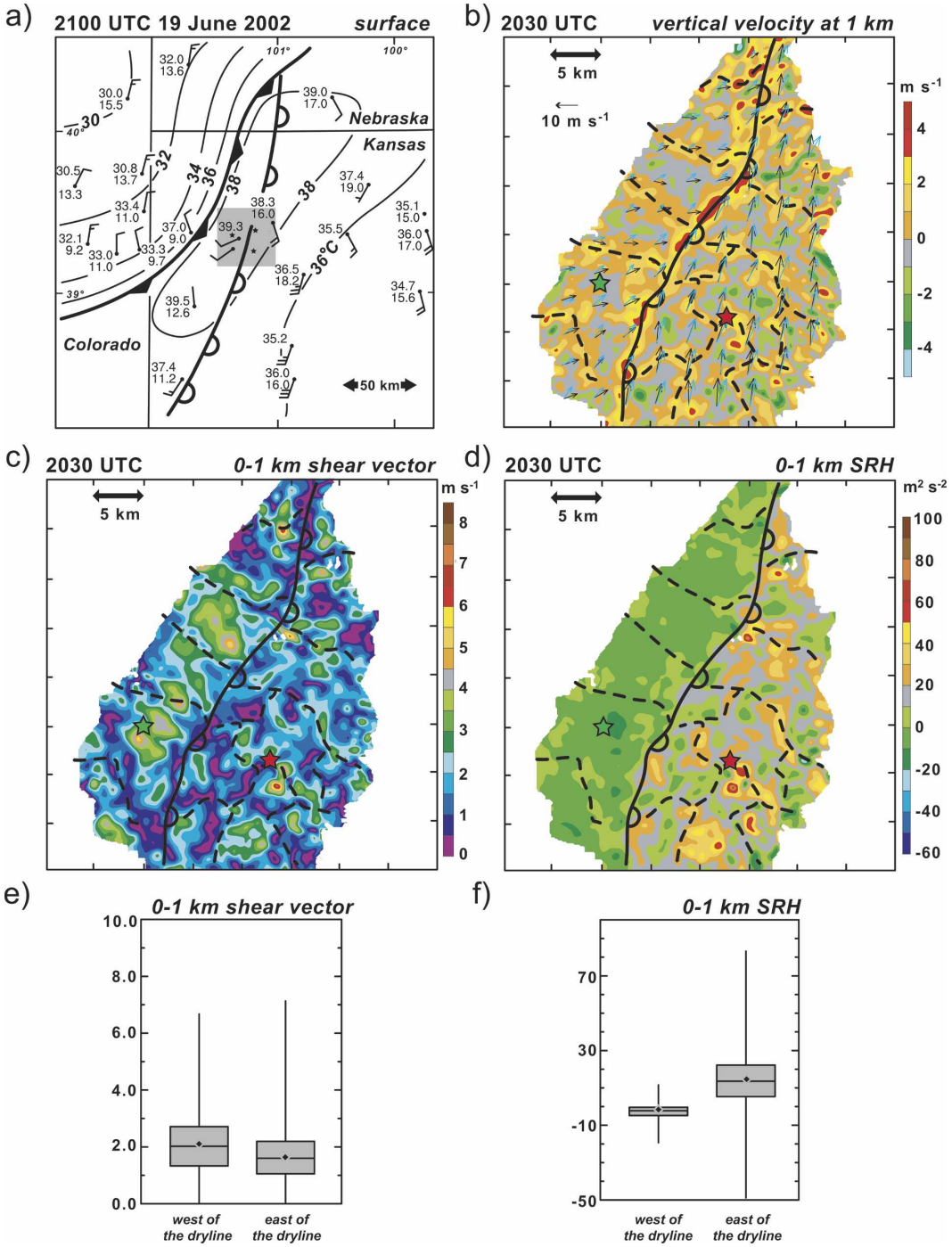

FIG. 4. Same as in Fig. 1, but 19 Jun 2002. The surface analysis is from 2100 UTC, and the vertical velocity, 0–1-km shear vector magnitude *S*, and SRH analyses are from 2030 UTC. The line with unfilled scallops indicates a dryline and the dashed lines indicate updrafts associated with horizontal convective rolls (HCRs). (b)–(d) The green and red stars indicate the locations of the hodographs displayed in Figs. 12g,h, respectively.

Greek X-band polarimetric (XPOL) radar (having specifications similar to the DOWs), and the Shared Mobile Atmospheric Research and Teaching (SMART) radar (Biggerstaff et al. 2005) was utilized during IHOP, although radar data were not available from all four radars for all of the analyses undertaken. The wavelength and stationary half-power beamwidth of the DOWs and XPOL are 3 cm and 0.93°, respec-

TABLE 1. Summary of dual-Doppler wind synthesis parameters. The time resolution of the wind syntheses is Δt; the horizontal and vertical grid spacing are Δx and Δz, respectively; the coarsest data spacing in the synthesis domain is Δd; and the Barnes smoothing parameter is κ.

Date	No. of radars	Domain dimensions (km)	Δt (s)	Δx, Δz (km)	Δd (km)	κ (km2)
10 Jun 2002	3–4	25 × 25	90	0.10, 0.10	0.39	0.26
12 Jun 2002	3–4	50 × 50	90	0.10, 0.10	0.45	0.36
14 Jun 2002	2	30 × 30	90	0.10, 0.10	0.40	0.29
19 Jun 2002	3	40 × 40	90	0.10, 0.10	0.43	0.32

tively, and, for the SMART radar, 5 cm and 1.5°, respectively. Volumes were completed every 90 s by the DOWs and XPOL and every 180 s by the SMART radar, during which time 15–16 elevation angles typically were scanned, ranging from 0.5° to 22°. The average horizontal and vertical data spacing within the analysis regions was approximately 200–300 m.

Radial velocity errors caused by low signal-to-noise ratio, second-trip echoes, sidelobes, ground clutter, and velocity aliasing were removed using the National Center for Atmospheric Research (NCAR) SOLO software prior to interpolating the data to a Cartesian grid in each case. Gridded radial velocity fields were produced by the NCAR REORDER software. A horizontal and vertical grid spacing of 100 m was used for all of the analyses. The lowest grid level was at the height of the mean radar elevation (more will be said about the implications of this choice near the end of this section). The objective analysis was accomplished using an isotropic, Gaussian, spherical weight function and smoothing parameter κ, as described by Barnes (1964). The values of κ ranged from 0.26 to 0.36 km^2, depending on the data spacing for each case. The choice of κ was based on the coarsest data sampling (Δd) within the wind synthesis domain, following the conservative recommendations of Trapp and Doswell (2000), whereby $\kappa = (1.33\Delta d)^2$ was used (Pauley and Wu 1990). Radial wind velocity structures having wavelengths less than 4 times the data spacing were severely damped by the objective analysis procedure.

Movement of features during the collection of a radar data volume was removed from the objectively analyzed radial velocity grids using Matejka's (2002) technique for determining the optimal reference frame velocity, although the objective analyses and ensuing wind syntheses were relatively insensitive to the translation speed because of the relative rapidity with which radar volumes were completed. Of course, differential translation within the domain is difficult to account for, but it is not believed that this effect significantly influenced the wind syntheses given the aforementioned insensitivity to the constant translation speed assumed. With the exception of the 14 June case, in which only two radars were used for the wind syntheses, the three-dimensional wind fields were synthesized using the overdetermined dual-Doppler approach in NCAR's Custom Editing and Display of Reduced Information in Cartesian Space software (e.g., Kessinger et al. 1987). The anelastic mass continuity equation (integrated upward) was used in all of the wind syntheses. The grid specifications and objective analysis parameters for each case are summarized in Table 1.

c. *Assessing the horizontal heterogeneity of vertical wind profiles*

Vertical wind profiles are commonly presented as hodographs. One challenge in describing the spatial and temporal variability of vertical wind profiles is that there are many ways to describe how hodographs differ. Hodograph differences can be defined as differences in hodograph length, shape, orientation, curvature, and how vertical wind shear is distributed along the hodograph. We have circumvented these difficulties by largely focusing on the variability of scalar fields (to be described below) that can be derived from the vertical wind profile, rather than trying to sensibly assess *hodograph* variability and relate it to boundary layer kinematic structures.

In the following section, the horizontal inhomogeneity of vertical wind profiles is portrayed by analyses of the magnitude of the 0–1-km vertical wind shear vector S and 0–1-km SRH (Davies-Jones et al. 1990), defined by

$$S = |\mathbf{v}_1 - \mathbf{v}_0|, \tag{1}$$

and

$$\mathrm{SRH} = -\int_{0\ \mathrm{km}}^{1\ \mathrm{km}} \mathbf{k} \cdot (\mathbf{v} - \mathbf{c}) \times \frac{\partial \mathbf{v}}{\partial z}\, dz, \tag{2}$$

respectively, where $\mathbf{v}(z) = [u(z), v(z)]$ is the horizontal wind velocity vector; $\mathbf{v}_0$ and $\mathbf{v}_1$ are the horizontal wind velocity vectors at the lowest grid level and 1 km above the lowest grid level, respectively; $\mathbf{c}$ is the storm motion vector [estimated using the Bunkers et al. (2000) tech-

nique based on IHOP mobile soundings];[2] z is the vertical coordinate; and **k** is the unit vector in the vertical direction.[3] The choice to present these particular parameters is arbitrary, of course. Our choice is influenced by the popularity of these parameters within the severe storms forecasting community (e.g., Thompson et al. 2003). We have every reason to believe that fields of other forecasting indices (e.g., Rasmussen and Blanchard 1998) are equally heterogeneous as those that are presented in the next section.

Last, we note that the references to wind velocities at a height of 0 km are somewhat casual. Such observations are at the lowest grid levels in the dual-Doppler wind syntheses. Because of radar horizon issues, the winds within roughly the lowest 100 m AGL are generally not well sampled; thus, wind velocities in this layer are synthesized from radial velocity measurements that have been extrapolated (downward) by the objective analysis. One might anticipate that the heterogeneity of the vertical wind profiles is perhaps underestimated in our dual-Doppler wind syntheses because the vertical wind shear is not well resolved in precisely the layer within which it tends to be largest (i.e., the lowest ~100 m AGL). (When in situ wind observations are used in the calculation of parameters such as S and SRH, the "surface" wind observation typically is at 10 m AGL.) On the other hand, the errors in the layer shear may be acceptably small given that comparisons between mobile mesonet (Straka et al. 1996) wind observations at 3 m AGL and dual-Doppler-derived winds at the lowest grid level interpolated to the mobile mesonet locations revealed that the mean absolute differences in wind speed (direction) were only approximately 1.3 m s^{-1} (5°) in the cases studied herein.

3. Observations of horizontal heterogeneity in the vertical wind shear fields

Fields of S and SRH derived from the multi-Doppler wind syntheses on the four case days are displayed in Figs. 1–4c,d. In some instances (e.g., 10 and 12 June) the S and SRH fields are highly correlated (linear correlation, $r > 0.8$). In other instances (e.g., west of the dryline on 19 June), the storm motion (a function of the wind over a depth far greater than that of the 0–1-km layer) is such that S and SRH are not well correlated.

What is more striking is the spatial complexity and heterogeneity of the S and SRH fields. For example, on 19 June values of S (SRH) range from 0.1 to 7.1 m s^{-1} (−49 to 84 m^2 s^{-2}) (Figs. 4e,f). Furthermore, the range of values increases as the depth of the layer over which the wind shear vector and SRH are computed increases. For example, values of S (SRH) computed in the 0–1-km layer on 12 June range from 0.1 to 4.4 m s^{-1} (−21 to 69 m^2 s^{-2}) (Figs. 2c,d), whereas values of S (SRH) range from 0.1 to 9.8 m s^{-1} (−61 to 180 m^2 s^{-2}) if computed over the 0–2-km layer (see Markowski and Richardson 2004).

Multiple scales of variability are apparent in the S and SRH fields in cases where mesoscale boundaries are present (10, 12, and 19 June). On 12 June, for example, in the easterly low-level flow north of an outflow boundary, S and SRH are larger on average than on the south (warm) side of the outflow boundary (Figs. 2e,f), probably as a result of baroclinic vorticity generation on the north side of the outflow boundary similar to that described by Markowski et al. (1998). In addition to this larger-scale variability, convective-scale (1–10 km) variability also is apparent within each air mass and is due to the perturbations in the horizontal wind components associated with boundary layer convection. In fact, in some of the cases in which mesoscale boundaries were present, the variability that can be attributed to boundary layer convection is as significant as that which can be attributed to the differing air masses. For example, in the 12 June case, the difference in the median S between the warm and cool sides of the outflow boundary was approximately half of the interquartile range (IQR) of the S values on the cool side of the boundary (Fig. 2e). The range of S (SRH) values observed on either side of the outflow boundary (not *across* the outflow boundary) spans >3 m s^{-1} (>50 m^2 s^{-2}), whereas the median S (SRH) values on either side of the outflow boundary differ by <1 m s^{-1} (<20 m^2 s^{-2}) (Figs. 2e,f). Similar observations were made in the 10 and 19 June cases, with respect to the relationships between the ranges of S and SRH values in each air mass and the difference in the median S and SRH values in each air mass (Figs. 1e,f and 4e,f), although for some parameters and cases [e.g., S on 10 June (Fig. 1e) and SRH on 19 June (Fig. 4f)], there is better separation between the IQRs of the parameters observed in

[2] The sensitivity of SRH to storm motion estimates is explored in the appendix.

[3] The $-\mathbf{k} \times \partial\mathbf{v}/\partial z$ term in (2) is an approximation for the horizontal vorticity vector, $\boldsymbol{\omega}_h = (\partial w/\partial y - \partial v/\partial z, \partial u/\partial z - \partial w/\partial x)$, where w is the vertical velocity and x and y are the horizontal coordinates. Following convention, the horizontal gradients of w are assumed to be much smaller than the vertical gradients of u and v, although this may not be guaranteed in a convective boundary layer characterized by weak vertical wind shear. Nevertheless, the SRH calculations performed herein make this approximation in order to be consistent with the method universally employed in an operational setting [i.e., that given by (2)].

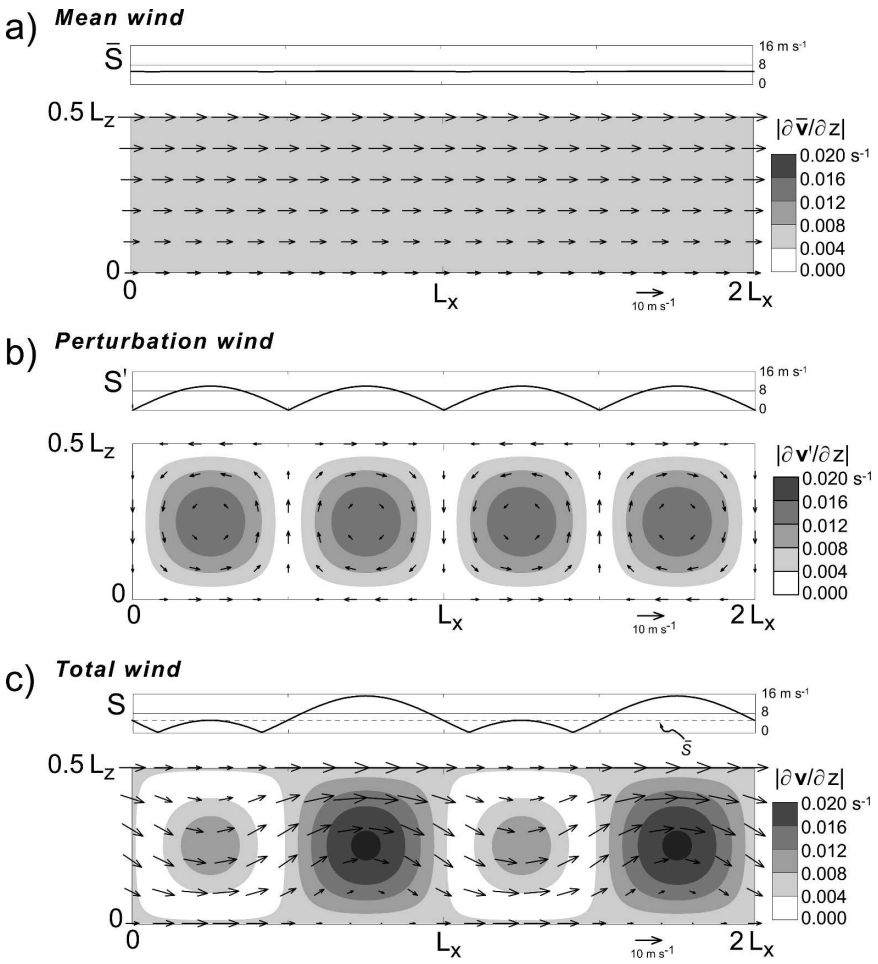

FIG. 5. Idealized case of horizontal rolls superimposed upon a unidirectional mean wind with constant shear, orthogonal to the roll axes (transverse rolls), illustrating the effects of the rolls on the local and mean vertical wind shear magnitude. (a) Mean wind field $\overline{\mathbf{v}}$ having a westerly wind shear vector. The wind vector lengths are proportional to the wind speed and $|\partial\overline{\mathbf{v}}/\partial z|$ is shaded (see the legend). The horizontal profile of $\overline{S}$ is also indicated, whereby $\overline{S} = |\overline{\mathbf{v}}_1 - \overline{\mathbf{v}}_0|$ is the magnitude of the mean wind shear vector between 0 and 1 km. (b) Perturbation wind field $\mathbf{v}'$ due to meridionally oriented rolls. The wind vector lengths are proportional to the wind speed and $|\partial\mathbf{v}'/\partial z|$ is shaded (see the legend). The horizontal profile of S' also is indicated, whereby $S' = |\mathbf{v}'_1 - \mathbf{v}'_0|$ is the magnitude of the perturbation wind shear vector between 0 and 1 km. (c) Total wind field, $\mathbf{v} = \overline{\mathbf{v}} + \mathbf{v}'$. The wind vector lengths are proportional to the wind speed and $|\partial\mathbf{v}/\partial z|$ is shaded (see the legend). The horizontal profile of S also is indicated, whereby $S = |\mathbf{v}_1 - \mathbf{v}_0|$ is the magnitude of the perturbation wind shear vector between 0 and 1 km. Note that $S \neq \overline{S} + S'$.

each air mass. In the 14 June case, in which no mesoscale boundaries are evident and wind speeds are unusually weak, S (SRH) values range from 0.0 to 3.1 m s^{-1} (-8 to 13 m^2 s^{-2}).

It is clear from Figs. 1–4 that the relationship between boundary layer drafts and vertical wind shear is difficult to generalize. The sign and magnitude of vertical wind shear fluctuations depend on the orientation of the mean flow and shear with respect to the orientation of the "perturbation" motions associated with the convection. To illustrate the effect of rolls on the total wind shear, idealized examples are depicted in Figs. 5–8, in which wind and wind shear perturbations due to two-dimensional horizontal rolls have been superimposed upon a unidirectional mean wind with constant shear, having orientations orthogonal ("transverse rolls"), parallel ("longitudinal rolls"), and at a 45° angle to the roll axes. The rolls are oriented in the y direction, whereby the wind velocity perturbation, $\mathbf{v}' = (u', v', w')$, is given by

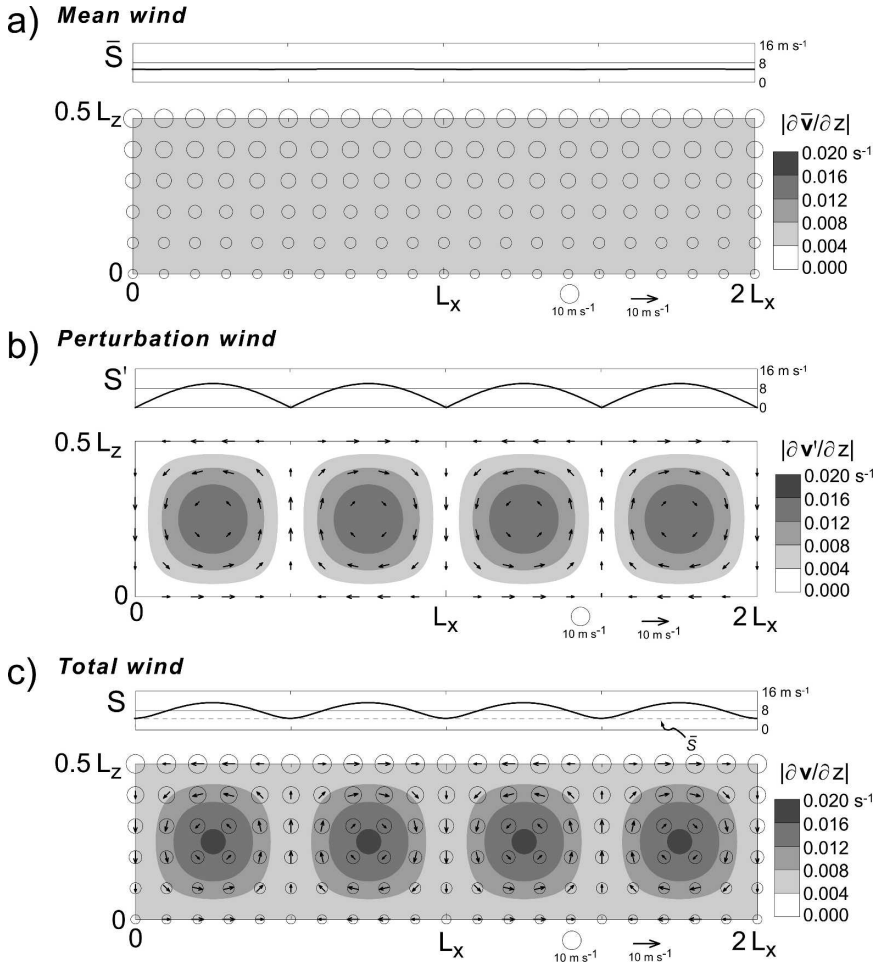

FIG. 6. Same as in Fig. 5, but for the case of horizontal rolls superimposed upon a unidirectional mean wind with constant shear, parallel to the roll axes (longitudinal rolls). The mean wind and mean wind shear vector are southerly (into the page). The circles indicate flow into the page, and the size of the circles is proportional to the wind speed (see the legend).

$$u'(x, z) = \hat{u} \sin\left(\frac{2\pi x}{L_x}\right) \cos\left(\frac{2\pi z}{L_z}\right), \tag{3}$$

$$v' = 0, \quad \text{and} \tag{4}$$

$$w'(x, z) = -\hat{w} \cos\left(\frac{2\pi x}{L_x}\right) \sin\left(\frac{2\pi z}{L_z}\right), \tag{5}$$

where $\hat{u}$ and $\hat{w}$ are the amplitudes of u' and w', respectively, and L_x and L_z are the horizontal and vertical wavelengths of the rolls, respectively. The mean wind, $\overline{\mathbf{v}} = (\overline{u}, \overline{v}, \overline{w})$, has constant vertical shear and is defined as

$$\overline{u}(z) = u_o + \frac{\partial \overline{u}}{\partial z} z, \tag{6}$$

$$\overline{v}(z) = v_o + \frac{\partial \overline{v}}{\partial z} z, \quad \text{and} \tag{7}$$

$$\overline{w} = 0, \tag{8}$$

where u_o and v_o are the zonal and meridional wind speeds at the ground, respectively, and $\partial\overline{u}/\partial z$ and $\partial\overline{v}/\partial z$ are the mean zonal and meridional wind shear, respectively. The total wind is $\mathbf{v} = \overline{\mathbf{v}} + \mathbf{v}'$. For the rolls appearing in Figs. 5–8, $L_x = L_z = 1000$ m and $\hat{u} = \hat{w} = 5$ m s^{-1}.[4] In the transverse rolls example (Figs. 5, 8a), a westerly mean shear vector is specified, whereby $u_o = 5$ m s^{-1}, $\partial\overline{u}/\partial z = 0.005$ s^{-1}, $v_o = 0$ m s^{-1}, and $\partial\overline{v}/\partial z = 0$ s^{-1}. In the longitudinal rolls example (Figs. 6, 8b), a southerly mean shear vector is specified, whereby $u_o = 0$

[4] Note that the aspect ratio of the rolls (horizontal scale divided by depth scale) is smaller than in theoretical predictions (e.g., Chandrasekhar 1961, p. 43) and observations (e.g., LeMone 1973), but that our specification of the roll dimensions in this simple demonstration does not affect the spatial relationship between vertical wind shear perturbations and wind velocity perturbations.

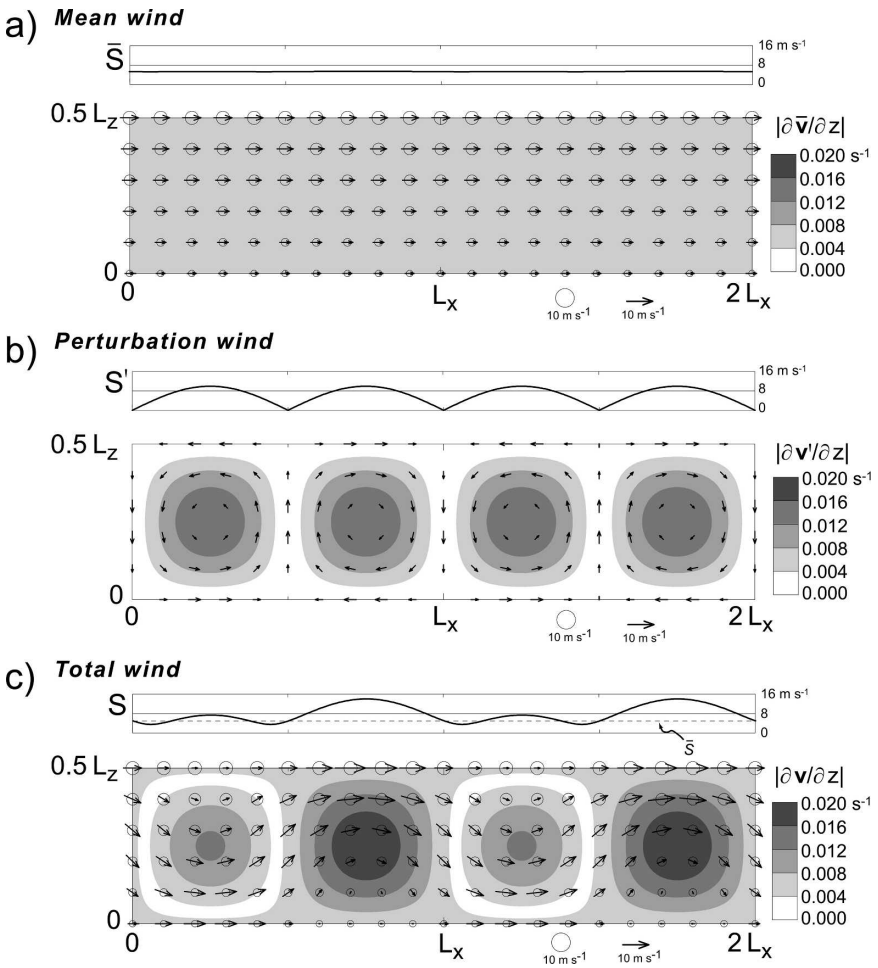

FIG. 7. Same as in Fig. 5, but for the case of horizontal rolls superimposed upon a unidirectional mean wind with constant shear, oriented at a 45° angle with respect to the roll axes. The mean wind and mean wind shear vector are southwesterly (into the page and toward the right). The circles indicate flow into the page, and the size of the circles is proportional to the wind speed (see legend).

$m\,s^{-1}$, $\partial\overline{u}/\partial z = 0.000\,s^{-1}$, $v_o = 5\ m\,s^{-1}$, and $\partial\overline{v}/\partial z = 0.005\,s^{-1}$. In the case of rolls oriented at a 45° angle with respect to the mean shear vector (Figs. 7, 8c), a southwesterly mean shear vector is specified, whereby $u_o = 5\cos(\pi/4)\ m\,s^{-1}$, $\partial\overline{u}/\partial z = 0.005\cos(\pi/4)\,s^{-1}$, $v_o = 5\sin(\pi/4)\ m\,s^{-1}$, and $\partial\overline{v}/\partial z = 0.005\sin(\pi/4)\,s^{-1}$.

Figures 5–8 reveal that, regardless of roll orientation, relative maxima in S are collocated with vertical velocity *magnitude* minima. Relative minima in S are located near vertical velocity magnitude maxima. The largest enhancement of S by rolls occurs when they are orthogonal to the mean shear (transverse rolls), in which case the maximum S values are located a quarter-wavelength downshear (upshear) of updrafts (downdrafts) (Figs. 5c, 8a). The largest reduction of S also occurs in the transverse rolls case near the aforementioned vertical velocity magnitude maxima. In contrast, for longitudinal rolls, S is equally enhanced where vertical velocity magnitudes are a minimum (Figs. 6c, 8b), although the magnitude of the enhancement is not as large as the maximum enhancement in the transverse rolls case (Figs. 5c, 8a). When the rolls are oriented at a 45° angle with respect to the mean wind shear vector, the horizontal distribution of S (Figs. 7c, 8c) falls between the S distributions of the transverse rolls and longitudinal rolls cases (Figs. 5c, 6c, 8a,b). The peak enhancement of S also occurs a quarter-wavelength downshear (upshear) of the roll updrafts (downdrafts) (Figs. 7c, 8c), with the amplitude of the enhancement being greater than that in the longitudinal rolls case (Figs. 6c, 8b), but less than that in the transverse rolls case (Figs. 5c, 8a).

The idealizations in Figs. 5–8 are slightly unrealistic because roll orientation is not arbitrary. Instead, roll

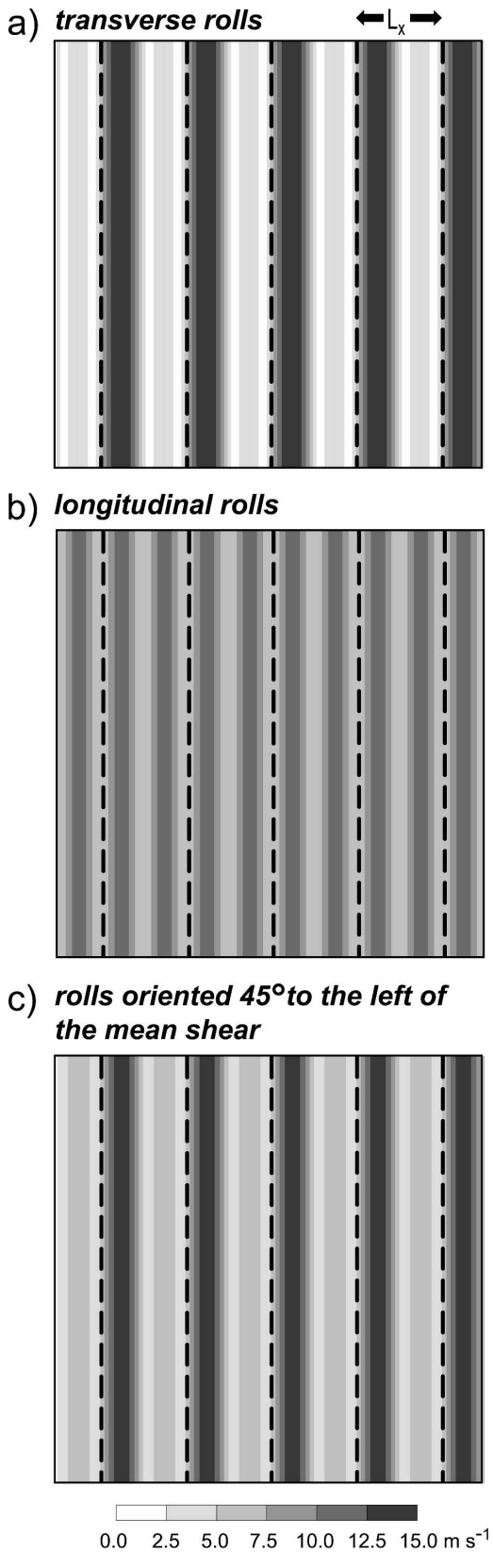

orientation depends on the relative importance of thermal and dynamical instabilities, the latter of which is sensitive to the details of the mean wind profile, such as its curvature (e.g., Cotton and Anthes 1989, 401–405). Nonetheless, even though the idealized mean wind profiles are not perfectly consistent with all of the specified roll orientations (e.g., rolls would not be expected to be orthogonal to the mean shear vector for a constant shear, undirectional wind profile in a boundary layer in which thermal instability is contributing to the convective overturning), we believe that the effects of a superpositioning of a mean, sheared flow and two-dimensional convective rolls on the total wind shear fields, as illustrated in Figs. 5–8, remain qualitatively valid despite their simplicity.

When the organization of boundary layer convection is not two dimensional, as is commonly observed, the superpositioning of a mean, sheared flow and boundary layer convection leads to a more complex relationship between boundary layer drafts and vertical wind shear than those in Figs. 5–8. The relationship between boundary layer drafts and SRH is no easier to generalize owing to the additional dependence of SRH perturbations on storm motion. Figure 9 shows the relationship between the vertical velocity and S fields for the case of hexagonal convective cells in the absence of mean wind shear (Fig. 9a) and in the presence of weak mean wind shear (0.003 s^{-1}; Fig. 9b). The idealized wind field is that which has been attributed to Christopherson (1940; see Emanuel 1994, p. 60). Though close scrutiny of Figs. 1–4 indicates that the actual boundary layer contains a complex arrangement of cell and finite-length rolls, the idealizations in Figs. 8 and 9 hold approximately at least for proximate groupings of boundary layer updrafts.

4. Time evolution of hodographs

Assuming a nonzero mean wind, the large spatial heterogeneity documented in section 3 implies large

←

FIG. 8. Horizontal cross sections of 0–1-km shear vector magnitude S for the three roll orientations depicted in vertical cross sections in Figs. 5–7 (see the text for descriptions of the analytic wind profiles). Updraft maxima are indicated by the heavy dashed lines. North is at the top. Horizontal rolls superimposed upon (a) a unidirectional, westerly mean wind with constant shear, orthogonal to the roll axes (transverse rolls), (b) a unidirectional, southerly mean wind with constant shear, parallel to the roll axes (longitudinal rolls), and (c) a unidirectional, southwesterly mean wind with constant shear, oriented at a 45° angle with respect to the roll axes.

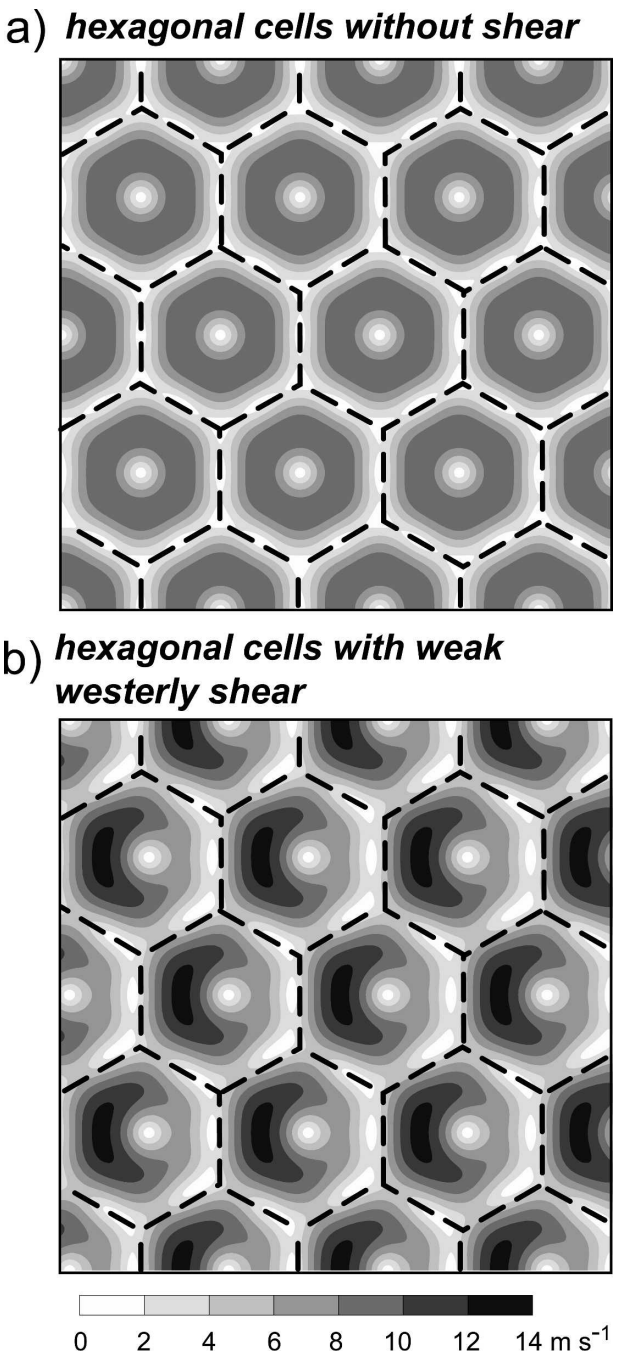

FIG. 9. Same as in Fig. 8, but for boundary layer convection organized as hexagonal cells when there is (a) no mean shear present and (b) weak, westerly mean shear of 0.003 s^{-1} present.

temporal variability in the characteristics of vertical wind profiles at fixed locations (temporal variability in the vertical wind profiles can also arise, of course, in the absence of a mean wind if the kinematic fields associated with the boundary layer convection evolve in time). Hodographs drawn from the vertical wind profiles at randomly selected grid points in the 14 June (weak mean wind) and 19 June (strong mean wind) cases are displayed at 3-min intervals over 9-min periods to demonstrate typical temporal changes in the hodograph as a function of the mean wind speed (Fig. 10; locations are indicated by the green stars in Figs. 3 and 4). The examples presented in Fig. 10 represent fairly typical hodograph changes on ~10-min time scales for those cases. Much more extreme temporal changes in the hodograph were occasionally observed in each case [not shown; a few additional examples are presented by Markowski and Richardson (2004)], especially when the effect of translation of the kinematic fields was augmented by rapid evolution.

As one would generally expect to be the case based on the differences in mean wind speed, much more significant temporal changes are observed in the 19 June hodographs compared with those on 14 June. The hodographs from the 14 June example (Fig. 10a) have a mean wind speed of approximately 1 m s^{-1}, whereas those in the 19 June example (Fig. 10b) have a mean wind speed of approximately 8 m s^{-1}. In the 14 June example, S (SRH) varies by <1 m s^{-1} (2 m^2 s^{-2}) over the 9-min period, whereas in the 19 June example, S (SRH) varies by ~1 m s^{-1} (12 m^2 s^{-2}). Although the temporal changes in S and SRH are larger in the 19 June example, one might still regard these changes as being relatively small. However, the variations in the orientation and curvature of the hodographs (not necessarily reflected by changes in S or SRH) over the 9-min period in the 19 June (Fig. 10b) example might be viewed as nontrivial by some, depending on the application.

5. Comments on "proximity soundings"

Since shortly after computing advancements allowed for the three-dimensional simulation of thunderstorms, so-called proximity soundings have been used to initialize numerical models in which the base state is horizontally homogeneous. Proximity soundings are intended to be representative of the ambient environment of the storm and have been obtained from either a single, fortuitous rawinsonde or by compositing several individual soundings launched at various ranges from a storm. Probably the most heavily used proximity sounding in numerical simulation studies represents the environment of the Del City, Oklahoma, supercell on 20 May 1977 (Klemp et al. 1981; Klemp and Rotunno 1983; Grasso and Cotton 1995; Adlerman et al. 1999; Adlerman and Droegemeier 2002).

Many arguments have been made for the use of such proximity soundings to define horizontally homoge-

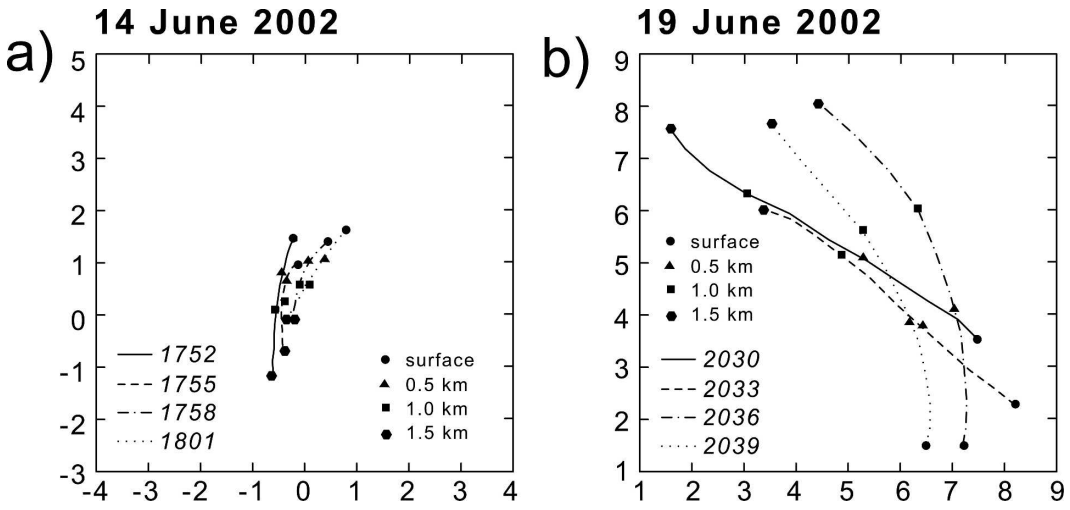

FIG. 10. (a) Hodographs at 1752, 1755, 1758, and 1801 UTC 14 Jun 2002 obtained from the location of the green star in Fig. 3. Units on the axes are m s^{-1}. The surface, 0.5, 1.0, and 1.5 km AGL locations on the hodograph traces are indicated with filled circles, triangles, squares, and pentagons, respectively. (b) Same as in (a), but for 2030, 2033, 2036, and 2039 UTC 19 Jun 2002. The hodographs were obtained from the location of the green star in Fig. 4.

neous base states. These arguments have included 1) the need to focus on the fundamental storm dynamics, which can most easily be accomplished if environmental heterogeneities are excluded; 2) lack of sufficiently detailed observations characterizing the heterogeneity; and 3) difficulties in introducing heterogeneities because of model imbalances that may result. We believe that the preceding justifications quite often have been valid, although we also share the concerns expressed by Brooks et al. (1994, 1996), with respect to the definition of "proximity" and the differences in soundings obtained by rawinsondes released relatively near to each other in space and time. As model resolution becomes finer and high-resolution "case study" or tornadogenesis simulations become favored over large parameter space studies, it may be more crucial to account for the complex interactions between storms and environmental heterogeneities. Indeed, Richardson (1999) and Richardson et al. (2007) showed significant changes in the structure of simulated convective storms due to movement through environments characterized by spatially varying vertical wind shear or moisture. Storm properties routinely exhibited a complex dependency on both their current environment and that over their history. In some cases, storm existence itself might not even be predicted based on only a sounding near the storm at that particular time. It might be worth noting that the spatial scale of the wind shear and moisture heterogeneity in Richardson's simulations was considerably larger than what is documented herein. The scale of the variability probably was large enough to be captured by today's observing systems or mesoscale forecast models.

The spatial and temporal variability of vertical wind profiles documented in sections 3 and 4 leads one to naturally wonder about the representativeness of proximity soundings derived from a single sounding or even from compositing several soundings. What is perhaps most disturbing is that considerable heterogeneity is present even *away from* the obvious mesoscale boundaries that may be detectable by today's observing systems; that is, much heterogeneity is present in regions that many investigators might have classified as "horizontally homogeneous" in the past.[5]

It is also problematic that the heterogeneity implies that a hodograph obtained from a rawinsonde launched at a given location is likely to deviate from the true hodograph, because rawinsondes provide neither instantaneous nor truly vertical wind profiles. We have attempted to document the hodograph errors due to rawinsonde drift through a heterogeneous boundary layer by constructing "pseudohodographs," which simulate the hodograph that would be traced by a rawinsonde. A pseudohodograph was created at every other grid point by computing the trajectory[6] that a balloon would take through the boundary layer. The horizontal wind components at each level were ob-

[5] It is possible that the turbulence in these regions would be considered horizontally homogeneous in the statistical sense. In this section, we are concerned with point-to-point variability as experienced by a rawinsonde, rather than the statistical properties of the perturbations.

[6] Trajectories were computed using a fourth-order Runge–Kutta integration algorithm and a time step of 5 s.

tained by measuring the displacement of the hypothetical balloon in a 5-s time period, which approximately emulates the frequency at which navigational data are recorded by rawinsondes. Given an assumed balloon ascent rate of 5 m s^{-1}, each pseudohodograph calculation typically required 4–5 three-dimensional wind syntheses spanning 300–400 s. As was the case for the true hodographs, the pseudohodographs only span the lowest 1.5 km.

The differences between the pseudohodographs and true hodographs in terms of *S* and SRH are summarized in Fig. 11. Figure 11 also includes the differences in terms of the 0–1-km hodograph length, which sometimes is referred to as "mean shear" when normalized by the depth over which the hodograph length has been measured (e.g., Rasmussen and Wilhelmson 1983). Hodograph length is more sensitive to the finescale structure of a hodograph (due to the fractal nature of a hodograph) than is *S* or SRH, and therefore perhaps better reflects the differences between the pseudohodographs and true hodographs.

The differences between the pseudohodographs and true hodographs are largest when significant evolution of the wind field occurs during the ascent of the balloon, and when the wind is such that the balloon traverses large gradients in horizontal wind as it ascends. Figure 12 displays examples of true and pseudohodographs where the differences between them are "typical," at least in terms of the *S* and SRH differences between them (within 1% of the median *S* and SRH differences; refer to Figs. 11a,b), in addition to examples of true and pseudohodographs that have "atypical" differences in terms of *S* and SRH (differences were at or above the 95th percentile in terms of *S* and SRH; again refer to Figs. 11a,b). Although the differences between the pseudohodographs and true hodographs generally may not be what one would consider to be large (e.g., >90% of all of the pseudohodographs had *S* values within 1 m s^{-1} of those computed from the true hodographs), at some "unlucky" locations, the differences are alarming (e.g., Figs. 12b,d, f,g), with *S* (SRH) differences >2 m s^{-1} (>40 m^2 s^{-2}), which amount to relative errors of up to 100% or more. Even where *S* and SRH differences suggest close similarity between the pseudohodographs and true hodograph, close inspection of the hodograph details can reveal differences in hodograph orientation or curvature that some might regard as nontrivial (e.g., Figs. 12a,c). The differences between the pseudohodographs and true hodographs, in addition to the real, ubiquitous heterogeneity documented in sections 3 and 4, illustrate a potential difficulty in directly comparing observed storm behaviors and the (observed) pseudosoundings

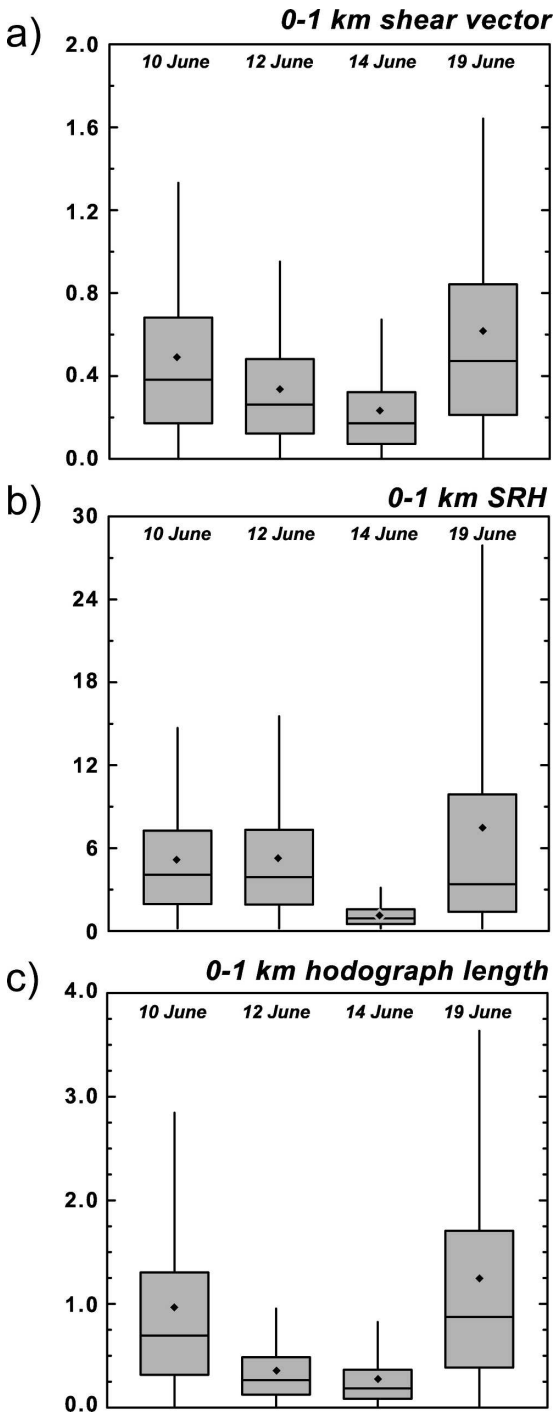

FIG. 11. Box-and-whisker plots of the absolute differences between the true hodographs and pseudohodographs in terms of (a) the 0–1-km shear vector magnitude *S*, (b) 0–1-km SRH, and (c) 0–1-km hodograph length for the 10, 12, 14, and 19 June cases. Because of the large skewness of the distributions of differences, the whiskers indicate the minimum and 95th percentile differences rather than the minimum and maximum differences (the maximum differences often were 50% larger than the 95th percentile differences). The small diamonds indicate mean differences.

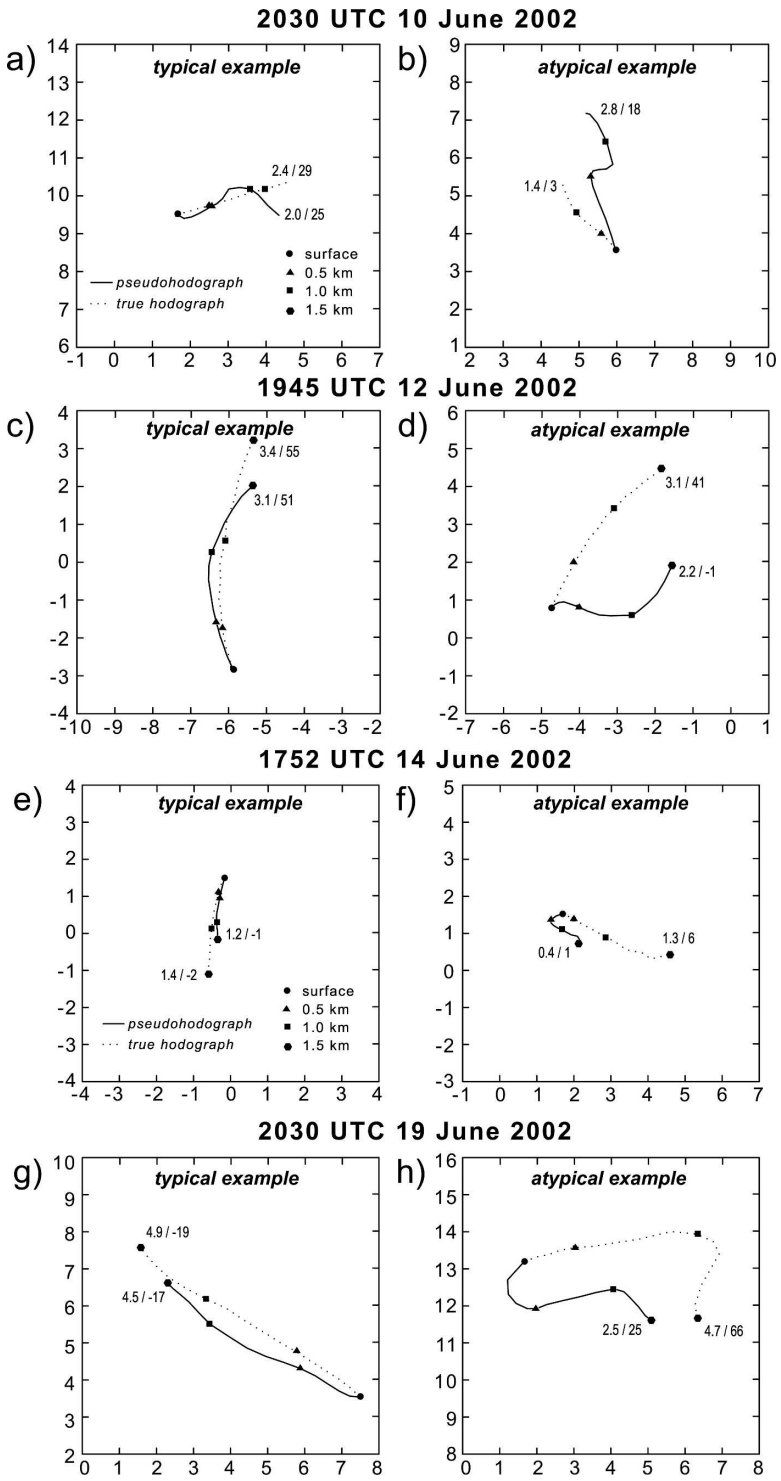

FIG. 12. Pseudohodographs and true hodographs at locations at which the differences, in terms of both *S* and SRH, were typical (within 1% of the median differences; refer to Figs. 11a,b) for that case, as well as at locations at which the differences between the pseudohodographs and true hodographs were atypical (differences were at or above the 95th percentile in terms of the magnitude of *S* and SRH; refer to Figs. 11a, b). Typical and atypical examples from (a), (b) 2030 UTC 10 Jun 2002; (c), (d) 1945 UTC 12 Jun 2002; (e), (f) 1752 UTC 14 Jun 2002; and (g), (h) 2030 UTC 19 Jun 2002. The typical and atypical examples were obtained at the locations of the green and red stars, respectively, indicated in Figs. 1, 2, 3, and 4. The pseudohodographs were obtained by assuming a balloon ascent rate of 5 m s^{-1}. Units on the axes are m s^{-1}. The surface, 0.5, 1.0, and 1.5 km AGL locations on the hodograph traces are indicated with filled circles, triangles, squares, and pentagons, respectively (for the 10 Jun 2002 case, data only extend to 1.3 km AGL). The pair of numbers appearing beside each pseudohodograph and true hodograph trace indicates the magnitude of the 0–1-km shear vector (m s^{-1}) and 0–1-km SRH (m^2 s^{-2}), respectively.

obtained from the storm environments, to storm behaviors predicted by simulation or theoretical studies based on true soundings.

6. Final remarks and future work

We caution the reader that, although small-scale wind shear variability has been documented herein, there are no clear means of applying these findings in severe storms forecasting or warning operations given the lack of real-time observations on these scales. Although past work has shown that moisture and wind shear variability on larger (meso β) scales can affect simulated storms, it is not known what impact, if any, variability on smaller (meso γ) scales has on actual storms, nor should the impact be inferred from the present study.

Some of our ongoing research activities are geared to further exploring the sensitivity of simulated convective storms to meso-β-scale moisture and wind shear variability (e.g., Kost and Richardson 2004; Kron 2004). Our future research plans include an investigation of how convective storms modify the kinematic heterogeneity present within convective boundary layers (e.g., beneath the leading anvil and within precipitation regions) using additional dual-Doppler radar observations. Ultimately we hope to develop a better understanding of how thermal-scale variability within the boundary layer impacts storms, if at all. Given the computing capabilities of today, we believe that it would be highly worthwhile to begin simulating storms with the inclusion of sensible heat fluxes and convective boundary layers (e.g., Carpenter et al. 1998), at least in high-resolution, "case study" or tornadogenesis simulations, although it may be challenging to do so in the translating domains that are typically utilized.

Acknowledgments. We are grateful to Nettie Arnott, Jim Marquis, Christina Hannon, and Brian Monahan for allowing us to use their dual-Doppler wind syntheses for this study, and to Conrad Ziegler and two anonymous reviewers for their insightful reviews. We also thank all of the IHOP planners and volunteers who facilitated the collection of the data relied upon for this study. This research was supported by National Science Foundation Grants ATM-0130307 and ATM-0208651 made to the Pennsylvania State University.

APPENDIX

Sensitivity of SRH to Storm Motion

In this appendix we explore the sensitivity of SRH to changes or uncertainty in storm motion. Following the form of (2), the SRH between the surface ($z = 0$) and $z = h$ is

$$\mathrm{SRH} = -\int_0^h \mathbf{k} \cdot (\mathbf{v} - \mathbf{c}) \times \frac{\partial \mathbf{v}}{\partial z}\, dz, \tag{A1}$$

$$= -\int_0^h \left[(u - c_x)\frac{dv}{dz} - (v - c_y)\frac{du}{dz} \right] dz, \tag{A2}$$

$$= \mathrm{GRH} + c_x \Delta v - c_y \Delta u, \tag{A3}$$

where $\mathbf{c} = (c_x, c_y)$ is the storm motion (assumed constant with height); Δu and Δv are the x and y components of $\mathbf{S}_{0h}$, which is the vertical shear vector between $z = 0$ and $z = h$; and GRH is the ground-relative helicity, whereby

$$\mathrm{GRH} = -\int_0^h \mathbf{k} \cdot \mathbf{v} \times \frac{\partial \mathbf{v}}{\partial z}\, dz. \tag{A4}$$

From (A3),

$$\delta\mathrm{SRH} = \delta c_x \Delta v - \delta c_y \Delta u, \tag{A5}$$

where δSRH is the sensitivity of SRH to storm motion uncertainty (or change) and $\delta\mathbf{c} = (\delta c_x, \delta c_y)$ is the storm motion uncertainty (or change). Equation (A5) also can be written as

$$\delta\mathrm{SRH} = \mathbf{k} \cdot \delta\mathbf{c} \times \mathbf{S}_{0h} = \delta\lambda |\mathbf{S}_{0h}|, \tag{A6}$$

where $\delta\lambda$ is the projection of $\delta\mathbf{c}$ in the direction normal to the shear vector $\mathbf{S}_{0h}$ (positive for motions more rightward with respect to the 0–h-km shear vector). In other words, *the uncertainty of SRH due to the uncertainty of the storm motion is a linear function of the 0–h-km shear vector magnitude and storm motion uncertainty normal to the shear vector*. As the 0-h-km shear vector increases in magnitude, SRH sensitivity to storm motion increases. Figure A1 graphically depicts the relationships among $\delta\mathbf{c}$, $\delta\lambda$, and $\mathbf{S}_{0h}$.

In the present paper, it is not possible to estimate the uncertainty of SRH due to the uncertainty of the storm motion because we do not have observations of the wind profile above the boundary layer other than a sounding or two, and, therefore, cannot adequately assess $\delta\lambda$. In other words, we do not have observations above the boundary layer with the same resolution as those within the boundary layer, thus we have no way of knowing whether storm motion changes might compensate somewhat for the horizontal heterogeneity of the hodograph (this question was raised by one of the reviewers). It does seem unlikely that variations in the wind profile within the lowest 1 km of just a few meters per second would have significant impact on the storm motion, given that the storm motion is some function of the wind profile over the *entire depth* of the storm.

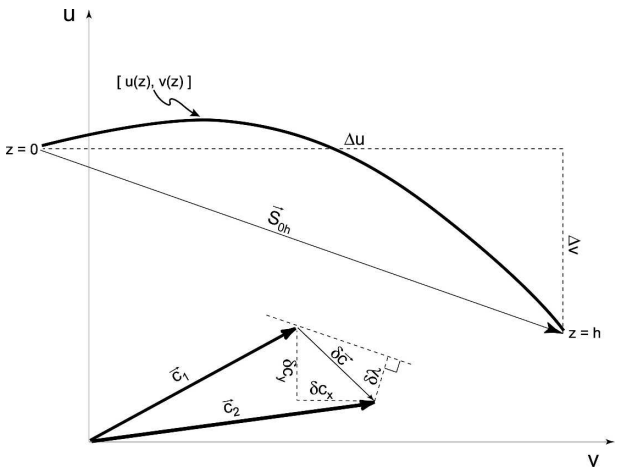

FIG. A1. Schematic diagram depicting the various aspects of a hodograph $[u(z), v(z)]$ that control the sensitivity of SRH to storm motion. The vectors $\mathbf{c}_1$ and $\mathbf{c}_2$ are two storm motions and the vector difference between them is $\delta\mathbf{c} = (\delta c_x, \delta c_y)$. The projection of $\delta\mathbf{c}$ in the direction normal to the shear vector drawn between $z = 0$ and $z = h$, $\mathbf{S}_{0h}$ $[=(\Delta u, \Delta v)]$, is $\delta\lambda$.

Furthermore, there is no observational evidence of which we are aware that shows storm motion changes on the space and time scales of the vertical wind profile variability documented herein. Overall, we believe that the SRH heterogeneity shown in Figs. 1–4 is largely insensitive to assumptions about storm motion as long as the assumptions are consistent across the domain.

REFERENCES

Adlerman, E. J., and K. K. Droegemeier, 2002: The sensitivity of numerically simulated cyclic mesocyclogenesis to variations in model physical and computational parameters. *Mon. Wea. Rev.,* **130,** 2671–2691.

——, ——, and R. Davies-Jones, 1999: A numerical simulation of cyclic mesocyclogenesis. *J. Atmos. Sci.,* **56,** 2045–2069.

Arnott, N., Y. Richardson, J. Wurman, and E. N. Rasmussen, 2006: Relationship between a weakening cold front, misocyclones, and cloud development on 10 June 2002 during IHOP. *Mon. Wea. Rev.,* **134,** 311–335.

Barnes, S. L., 1964: A technique for maximizing details in numerical weather map analysis. *J. Appl. Meteor.,* **3,** 396–409.

Biggerstaff, M. I., and Coauthors, 2005: The Shared Mobile Atmospheric Research and Teaching (SMART) radar: A collaboration to enhance research and teaching. *Bull. Amer. Meteor. Soc.,* **86,** 1263–1274.

Brooks, H. E., C. A. Doswell, and J. Cooper, 1994: On the environments of tornadic and nontornadic mesocyclones. *Wea. Forecasting,* **9,** 606–618.

——, M. T. Carr, and J. E. Ruthford, 1996: Preliminary analysis of soundings from VORTEX-95. Preprints, *18th Conf. on Severe Local Storms,* San Francisco, CA, Amer. Meteor. Soc., 133–136.

Bunkers, M. J., B. A. Klimowski, J. W. Zeitler, R. L. Thompson, and M. L. Weisman, 2000: Predicting supercell motion using a new hodograph technique. *Wea. Forecasting,* **15,** 61–79.

Carpenter, R. L., K. K. Droegemeier, and A. M. Blyth, 1998: Entrainment and detrainment in numerically simulated cumulus congestus clouds. Part I: General results. *J. Atmos. Sci.,* **55,** 3417–3432.

Chandrasekhar, S., 1961: *Hydrodynamic and Hydromagnetic Stability.* Oxford University Press, 652 pp.

Christopherson, D. G., 1940: Note on the vibration of membranes. *Quart. J. Math.,* **11** (Oxford Series), 63–65.

Cotton, W. R., and R. A. Anthes, 1989: *Storm and Cloud Dynamics.* Academic Press, 883 pp.

Davies-Jones, R. P., D. Burgess, and M. Foster, 1990: Test of helicity as a tornado forecast parameter. Preprints, *16th Conf. on Severe Local Storms,* Kananaskis Park, Alberta, Canada, Amer. Meteor. Soc., 588–592.

Emanuel, K. A., 1994: *Atmospheric Convection.* Oxford University Press, 580 pp.

Grasso, L. D., and W. R. Cotton, 1995: Numerical simulation of a tornado vortex. *J. Atmos. Sci.,* **52,** 1192–1203.

James, R. P., P. M. Markowski, and J. M. Fritsch, 2006: Bow echo sensitivity to ambient moisture and cold pool strength. *Mon. Wea. Rev.,* **134,** 950–964.

Kessinger, C. J., P. S. Ray, and C. E. Hane, 1987: The Oklahoma squall line of 19 May 1977. Part I: A multiple Doppler analysis of convective and stratiform structure. *J. Atmos. Sci.,* **44,** 2840–2864.

Klemp, J. B., and R. Rotunno, 1983: A study of the tornadic region within a supercell thunderstorm. *J. Atmos. Sci.,* **40,** 359–377.

——, R. B. Wilhelmson, and P. S. Ray, 1981: Observed and numerically simulated structure of a mature supercell thunderstorm. *J. Atmos. Sci.,* **38,** 1558–1580.

Kost, J., and Y. P. Richardson, 2004: The influence of temporally-varying vertical wind shear on numerically simulated convective storms. Preprints, *22d Conf. on Severe Local Storms,* Hyannis, MA, Amer. Meteor. Soc., CD-ROM, 9.2.

Kron, J., 2004: The evolution of numerically modeled convection in an environment containing horizontal variations of vertical shear and low-level moisture. M.S. thesis, Department of Meteorology, The Pennsylvania State University, 170 pp.

LeMone, M. A., 1973: The structure and dynamics of horizontal roll vortices in the planetary boundary layer. *J. Atmos. Sci.,* **30,** 1077–1091.

Markowski, P. M., and Y. P. Richardson, 2004: Multiple-Doppler radar observations of vertical wind profile heterogeneity in convective boundary layers. Preprints, *22d Conf. on Severe Local Storms,* Hyannis, MA, Amer. Meteor. Soc., CD-ROM, P13.1.

——, J. M. Straka, E. N. Rasmussen, and D. O. Blanchard, 1998: Variability of storm-relative helicity during VORTEX. *Mon. Wea. Rev.,* **126,** 2959–2971.

——, C. Hannon, and E. Rasmussen, 2006: Observations of convection initiation "failure" from the 12 June 2002 IHOP deployment. *Mon. Wea. Rev.,* **134,** 375–405.

Marquis, J. N., Y. P. Richardson, and J. M. Wurman, 2007: Kinematic observations of misocyclones along boundaries during IHOP. *Mon. Wea. Rev.,* in press.

Matejka, T., 2002: Estimating the most steady frame of reference from Doppler radar data. *J. Atmos. Oceanic Technol.,* **19,** 1035–1048.

McCaul, E. W., Jr., and M. L. Weisman, 2001: The sensitivity of simulated supercell structure and intensity to variations in the shapes of environmental buoyancy and shear profiles. *Mon. Wea. Rev.,* **129,** 664–687.

——, and C. Cohen, 2002: The impact on simulated storm structure and intensity of variations in the mixed layer and moist layer depths. *Mon. Wea. Rev.,* **130,** 1722–1748.

Murphey, H. V., R. M. Wakimoto, C. N. Flamant, and D. E. Kingsmill, 2006: The dryline on 19 June 2002 during IHOP. Part I: Airborne Doppler and LEANDRE II analyses of the thin line structure and convection initiation. *Mon. Wea. Rev.,* **134,** 406–430.

Pauley, P. M., and X. Wu, 1990: The theoretical, discrete, and actual response of the Barnes objective analysis scheme for one- and two-dimensional fields. *Mon. Wea. Rev.,* **118,** 1145–1163.

Rasmussen, E. N., and R. B. Wilhelmson, 1983: Relationships between storm characteristics and 1200 GMT hodographs, low-level shear, and stability. Preprints, *13th Conf. on Severe Local Storms,* Tulsa, OK, Amer. Meteor. Soc., J5–J8.

——, and D. O. Blanchard, 1998: A baseline climatology of sounding-derived supercell and tornado forecast parameters. *Wea. Forecasting,* **13,** 1148–1164.

——, J. M. Straka, R. P. Davies-Jones, C. A. Doswell, F. H. Carr, M. D. Eilts, and D. R. MacGorman, 1994: Verification of the Origins of Rotation in Tornadoes Experiment: VORTEX. *Bull. Amer. Meteor. Soc.,* **75,** 995–1006.

Richardson, Y. P., 1999: The influence of horizontal variations in vertical shear and low-level moisture on numerically simulated convective storms. Ph.D. dissertation, University of Oklahoma, Norman, Oklahoma, 236 pp.

——, J. Marquis, E. N. Rasmussen, J. M. Wurman, and N. R. Arnott, 2004: Analysis of convection initiation along a dryline on 19 June 2002. Preprints, *22d Conf. on Severe Local Storms,* Hyannis, MA, Amer. Meteor. Soc., CD-ROM, 16A.4.

——, K. K. Droegemeier, and R. P. Davies-Jones, 2007: The influence of horizontal environmental variability on numerically simulated convective storms. Part I: Variations in vertical shear. *Mon. Wea. Rev.,* in press.

Stonitsch, J. R., and P. M. Markowski, 2007: Unusually long-duration, multiple-Doppler radar observations of a front in a convective boundary layer. *Mon. Wea. Rev.,* **135,** 93–117.

Straka, J. M., E. N. Rasmussen, and S. E. Fredrickson, 1996: A mobile mesonet for finescale meteorological observations. *J. Atmos. Oceanic Technol.,* **13,** 921–936.

Thompson, R. L., R. Edwards, J. A. Hart, K. L. Elmore, and P. M. Markowski, 2003: Close proximity soundings within supercell environments obtained from the Rapid Update Cycle. *Wea. Forecasting,* **18,** 1243–1261.

Trapp, R. J., and C. A. Doswell III, 2000: Radar data objective analysis. *J. Atmos. Oceanic Technol.,* **17,** 105–120.

Weckwerth, T. M., J. W. Wilson, and R. M. Wakimoto, 1996: Thermodynamic variability within the convective boundary layer due to horizontal convective rolls. *Mon. Wea. Rev.,* **124,** 769–784.

——, ——, ——, and N. A. Crook, 1997: Horizontal convective rolls: Determining the environmental conditions supporting their existence and characteristics. *Mon. Wea. Rev.,* **125,** 505–526.

——, and Coauthors, 2004: An overview of the International H_2O Project (IHOP) and some preliminary highlights. *Bull. Amer. Meteor. Soc.,* **85,** 253–277.

Wurman, J., J. Straka, E. Rasmussen, M. Randall, and A. Zahrai, 1997: Design and deployment of a portable, pencil-beam, pulsed, 3-cm Doppler radar. *J. Atmos. Oceanic Technol.,* **14,** 1502–1512.